1-23-2018

Metastable Ar(1s₅) Density Dependence on Pressure and Argon-helium Mixture in a High Pressure Radio Frequency Dielectric Barrier Discharge

Daniel J. Emmons
Air Force Institute of Technology

David E. Weeks
Air Force Institute of Technology

Ben Eshel
Air Force Institute of Technology

Glen P. Perram
Air Force Institute of Technology

Recommended Citation

Metastable $Ar(1s_5)$ density dependence on pressure and argon-helium mixture in a high pressure radio frequency dielectric barrier discharge ⊘

D. J. Emmons ; D. E. Weeks ; B. Eshel ; G. P. Perram

CrossMark

View Online

Export Citation

Metastable Ar$(1s_5)$ density dependence on pressure and argon-helium mixture in a high pressure radio frequency dielectric barrier discharge

D. J. Emmons,[a] D. E. Weeks, B. Eshel, and G. P. Perram
Department of Physics, Air Force Institute of Technology, 2950 Hobson Way, Wright-Patterson AFB, Ohio 45433, USA

Simulations of an α-mode radio frequency dielectric barrier discharge are performed for varying mixtures of argon and helium at pressures ranging from 200 to 500 Torr using both zero and one-dimensional models. Metastable densities are analyzed as a function of argon-helium mixture and pressure to determine the optimal conditions, maximizing metastable density for use in an optically pumped rare gas laser. Argon fractions corresponding to the peak metastable densities are found to be pressure dependent, shifting from approximately 15% Ar in He at 200 Torr to 10% at 500 Torr. A decrease in metastable density is observed as pressure is increased due to a diminution in the reduced electric field and a quadratic increase in metastable loss rates through Ar_2^* formation. A zero-dimensional effective direct current model of the dielectric barrier discharge is implemented, showing agreement with the trends predicted by the one-dimensional fluid model in the bulk plasma. https://doi.org/10.1063/1.5009337

I. INTRODUCTION

Optically pumped rare gas lasers (OPRGLs) that employ Ar as the lasing medium require sufficient production of metastable $Ar(1s_5)$ to act as the lowest energy species of the laser system.[1] Diode pumping from $Ar(1s_5)$ to $Ar(2p_9)$ followed by rapid collisional relaxation from $Ar(2p_9)$ to $Ar(2p_{10})$ allows for a population inversion and subsequent lasing to $Ar(1s_5)$. The dependence of diode laser absorption and optical gain on $Ar(1s_5)$ densities[2,3] requires metastable densities on the order of 10^{13} cm^{-3} at atmospheric pressures to produce output laser intensities above 100 W/cm^2 for an active medium length of 1.9 cm (Ref. 1). Near-atmospheric pressures help to match the diode laser bandwidth to the $Ar(1s_5) + \hbar\omega \rightarrow Ar(2p_9)$ absorption linewidth and increase the non-adiabatic transition rate from $Ar(2p_9)$ to $Ar(2p_{10})$. Thermal instabilities are problematic at these higher pressures,[4–6] but radio frequency (RF) dielectric barrier discharges (DBDs) are able to maintain stability due to a limited ionization period occurring near the cycle peaks, which corresponds to an increased energy threshold for instability formation.[7]

Previous kinetic analyses of Ar-He mixtures in an OPRGL have been performed to find the optimal Ar-fraction and pressure for laser efficiency. One kinetic study[3] analyzed laser efficiency as a function of pressure and Ar-He composition for a non-specific discharge scenario, concluding that a mixture of approximately 1% Ar in He results in the largest total efficiency, defined as the output power divided by the sum of discharge and pump powers. A separate OPRGL kinetic analysis found the peak optical conversion efficiency (output laser intensity divided by the absorbed pump intensity) to occur at He partial pressures below 1.5 atm for an Ar partial pressure of 20 Torr.[8] An experimental and computational analysis of microwave resonator-driven microplasmas at a variety of Ar-He mixtures and pressures ranging from

100 to 730 Torr found that an Ar-fraction near 5% at a pressure of 100 Torr produces the largest metastable densities.[9] Additionally, peak metastable densities were found to decrease as the discharge pressure was increased.

An earlier analysis of a pulsed direct current (DC) discharge using a 7% Ar in He mixture at a pressure of 270 Torr provided insight into the kinetics controlling metastable behavior over a single pulse.[10] The analysis developed a robust reaction rate package centered around the species vital to OPRGL operation. In this paper, we use the same reaction rate package to calculate the $Ar(1s_5)$ density as a function of argon-helium mixture and pressure for an RF-DBD. Simulated fluorescence from a one-dimensional fluid model is compared with experiment along the centerline of the discharge cavity. A zero-dimensional kinetic model is developed, reducing the problem to an effective DC discharge. The zero and one-dimensional simulations are compared in the center of the discharge cavity showing close agreement between the two approaches. Due to the relatively large computational time required for the one-dimensional RF-DBD simulations, the use of the zero-dimensional approach is preferable in the bulk plasma where the model is appropriate.

II. EXPERIMENT

Plasma fluorescence is collected using a Point Grey Grasshopper (GS3-Y3-32S4m-C) USB 3.0 camera with a 3.45 μm pixel pitch and a 1/1.8″ CMOS detector. The spectral sensitivity of the detector ranges from 300 to 900 nm. A Computar 50 mm aperture, variable focus, f 1:1.8 lens is used to image the center of the discharge. The camera was placed at one end of the tube at a distance of 35 cm from the midpoint with an f/# of 16. The optical system results in a resolution of 41 μm per pixel.

The plasma was produced in an RF-DBD discharge with a "clam-shell" electrode/dielectric structure where a 0.64 cm Pyrex tube (0.38 cm I.D.) is wrapped by two copper electrodes

a)Electronic mail: daniel.emmons@afit.edu

of 5.0 cm length. The electrodes were machined with a gap of 0.32 cm at the edges and a maximum gap of 0.64 cm at the center. Ultra-high purity (99.999%) Ar and He gases are filtered through an SAES high-flow rate filter (MC200–904FC) which reduces impurities to 100 parts-per-trillion, 2–3 orders of magnitude lower than the Ar* density. Figure 1 shows a view of the RF-DBD apparatus in (a) and a long exposure time end-on image from the Point Grey camera in (b) with no discharge.

An example of the images collected for a 10% Ar in He mixture at 300 Torr is displayed in Fig. 2. The yellow rectangle, 90×10 pixels or 3.69×0.41 mm, outlines the region in which the apparatus is most similar to a parallel plate configuration. These rows are averaged together to facilitate comparison to the simulations (as shown in Fig. 7). The bright outer region is caused by plasma emission that is reflected into the detector by the inner wall of the Pyrex tube.

III. MODELS

The discharge chamber modeled in this analysis consists of parallel plate electrodes separated by 6.4 mm with both electrodes covered by a 1.3 mm thick dielectric with a permittivity of $\epsilon_d = 5\epsilon_0$ (Fig. 3). This parallel plate geometry is used as an approximation to the centerline of the cylindrical geometry displayed in Fig. 2. Following Ref. 10, the list of species used to analyze OPRGL kinetics for a high pressure Ar-He mixture is $Ar(1s_5)$, $Ar(1s_4)$, $Ar(2p_{10})$, $Ar(2p_9)$, $Ar(2p_8)$, $Ar(h.l.)$, Ar_2^*, Ar_2^+, Ar^+, He^*, He_2^*, He_2^+, $HeAr^+$, and He^+. The reaction rate package includes electron impact, recombination, two-heavy-body, three-heavy-body, and radiative rate coefficients. Including radiation trapping, an effective A-coefficient of 1.7×10^5 s^{-1} is used for the $Ar(1s_4) \rightarrow Ar + \hbar\omega$ transition in this discharge geometry.[11] At near-atmospheric pressures, the magnitude of radiation trapping is assumed to be independent of pressure[12] and mixture.

Electron impact rate coefficients and transport parameters are calculated using BOLSIG+ (Ref. 13) where the rate coefficients for electron impact collisions are computed from the non-Maxwellian electron energy distribution function (EEDF) along with the reaction cross section. The EEDF is dependent on species densities and the reduced electric field,

FIG. 2. End-on image of an RF-DBD for a 10% Ar in He mixture at 300 Torr with an applied power of 10 W. The outer fluorescence is emission from the sheath that is reflected into the detector by the inner wall of the Pyrex tube. The yellow rectangle outlines the region that is averaged to form a one-dimensional fluorescence profile for comparison with simulations.

E/N, where N is the neutral gas density. A one-to-one mapping of E/N to the electron temperature, $T_e = 2\langle\epsilon\rangle/3$, where $\langle\epsilon\rangle$ is the average electron energy, provides a unique EEDF for a given T_e, allowing T_e to be used as a proxy for E/N during EEDF computation. Additionally, for a driving angular frequency of $\omega = 2\pi \times 13.56$ MHz in the pressure range of 200–500 Torr, the reduced angular frequency ω/N is on the order of 10^{-17} m^3/s, which allows the EEDFs to be calculated using a DC field.[13]

The EEDF dependence on the Ar-He mixture is displayed in Fig. 4 for an electron temperature of 2 eV. As the fraction of He is increased, the population of high-energy (above excitation and ionization thresholds) electrons increases, approaching a Maxwellian distribution. This increase in the population of high-energy electrons increases the Ar excitation and ionization rate coefficients. However, the electron excitation and ionization rates also depend on the Ar density, n_{Ar}, which increases with Ar-fraction. The $Ar(1s_5)$ excitation frequency,
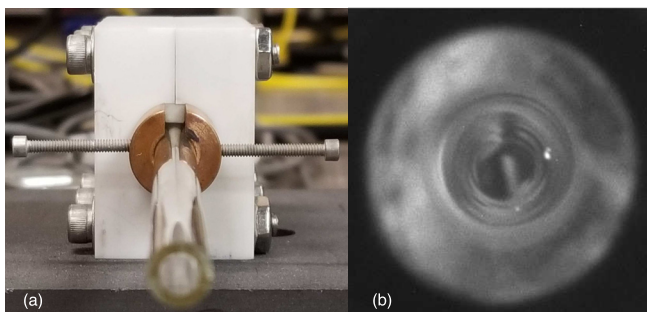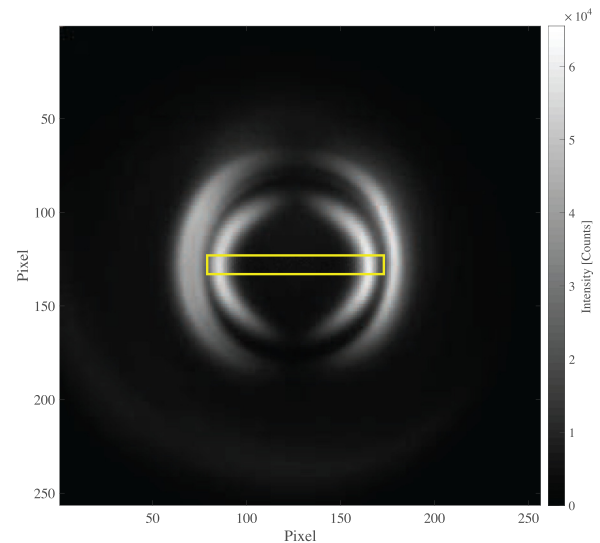

FIG. 1. (a) An end-on view of the RF-DBD apparatus. The 61 cm long Pyrex tube is sandwiched at the midpoint on the left and right by two copper electrodes that are 5 cm long and separated by 0.32 cm using an insulating Macor block. (b) A long exposure view down the Pyrex tube with no discharge. The unfocused region in the foreground is the face of the 0.13 cm thick tube wall. For this image and the image in Fig. 2, the camera was focused midway down the tube.
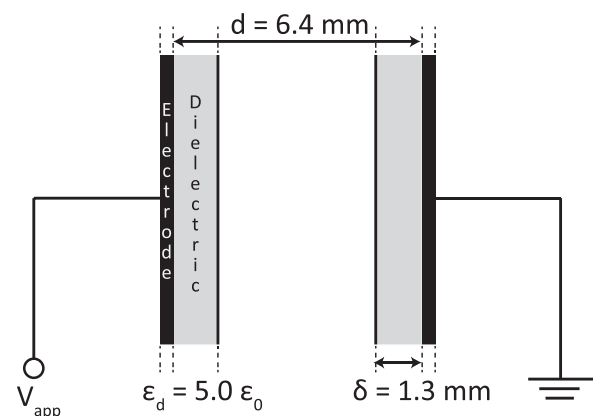

FIG. 3. A cross section of the simulated radio frequency dielectric barrier discharge chamber. The plates are assumed to be infinite in extent in the calculations.
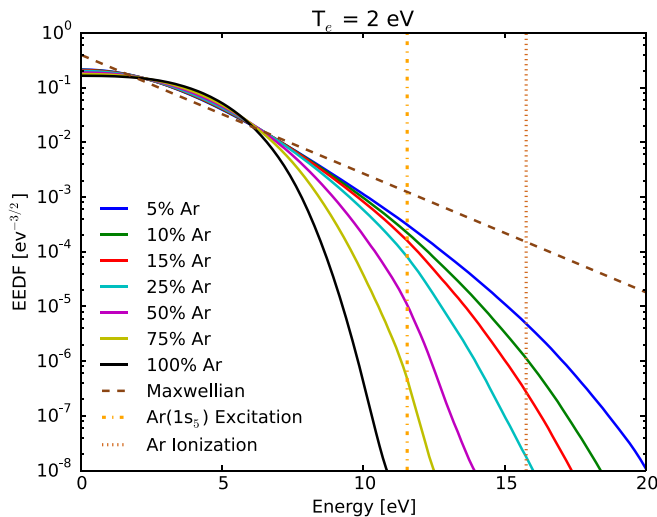
FIG. 4. Electron energy distribution functions for varying Ar-He mixtures with an electron temperature of 2 eV, as calculated by BOLSIG+.

FIG. 6. Electron temperatures mapped to reduced electric fields for varying Ar-He mixtures, as calculated by BOLSIG+.

ν_{exc}, is displayed in Fig. 5 as a function of electron temperature where $\nu_{exc} = k_{exc}n_{Ar}$, and k_{exc} is the rate coefficient for $Ar + e^- \rightarrow Ar(1s_5) + e^-$. At a pressure of 200 Torr, the maximum excitation frequency shifts to larger Ar-fractions for $T_e > 3$ eV. For $T_e < 3$ eV, the lower Ar-fractions have elevated excitation frequencies due to the increased population of high-energy electrons.

The reduced electric field as a function of T_e is displayed in Fig. 6 where E/N magnitudes of approximately 5 Td, typical of the bulk plasma at steady-state, correspond to elevated electron temperatures as the Ar-fraction increases. These larger values of T_e are caused by a reduction in the EEDF for energies below ~3 eV as the Ar-fraction becomes larger (Fig. 4). The loss in low energy electrons is compensated by increasing the EEDF population at energies just below the excitation threshold, which increases the distribution average. However, the EEDF population at energies above the excitation and ionization thresholds is also decreased as the Ar-fraction is increased. As a result, the increase of T_e with
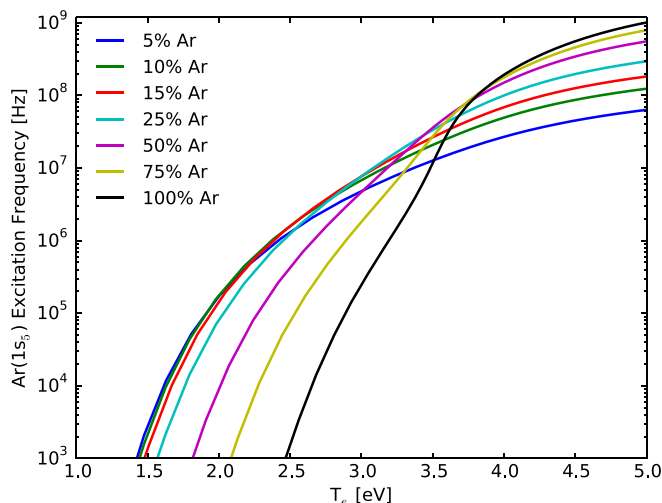
Ar-fraction at $E/N \approx 5$ Td does not correspond to an increase in excitation or ionization rate coefficients.

Electron mobilities and diffusion coefficients are also calculated using BOLSIG+. Ion mobilities are taken from Ward[14] along with an application of Blanc's Law[15,16] to determine the mobility in an Ar-He mixture. Following the measurements of Ref. 17, all Ar ion species are assumed to have the same mobility as Ar^+, and all He ions are assumed to have the mobility of He^+. Additionally, the mobility of Ar^+ in He is assumed to be equal to the mobility of He^+ in He, and He ion mobilities are held constant over Ar-He mixtures.

A fluid approach[18–22] outlined in Ref. 10 is used to model the discharge in one-dimension, employing the Scharfetter and Gummel[23] finite volume scheme. Due to charge collection at the dielectric boundaries, an additional boundary condition must be implemented for Poisson's equation

$$\mathbf{n} \cdot (\epsilon_0 \mathbf{E}_1 - \epsilon_d \mathbf{E}_2) = \sigma_s, \qquad (1)$$

$$\frac{d\sigma_s}{dt} = \mathbf{n} \cdot \mathbf{j}_e + \mathbf{n} \cdot \mathbf{j}_p, \qquad (2)$$

where $\mathbf{n}$ is the outward normal vector to the boundary (dielectric), $\mathbf{E}_1$ is the electric field inside the discharge cavity, $\mathbf{E}_2$ is the electric field in the dielectric, ϵ_d is the dielectric permittivity, σ_s is the surface charge density, $\mathbf{j}_e$ is the electron current density to the dielectric surface, and $\mathbf{j}_p$ is the ion current density to the dielectric surface.

In addition to the one-dimensional fluid model, we also develop a simplified zero-dimensional approach to the RF discharge where the root-mean-square (RMS) voltage is treated as an effective DC voltage.[7] This treats the bulk region of the RF-DBD discharge as an effective DC discharge, which greatly reduces the required computation time. The zero-dimensional effective DC model is implemented through ZDPlasKin (Zero-Dimensional Plasma Kinetics) and models the kinetics of the bulk plasma by numerically integrating the system of reaction rate equations over time.[24] The zero-dimensional model implemented here calculates the bulk plasma voltage following the methods outlined by Raizer, Shneider, and Yatsenko.[7] To treat

FIG. 5. Metastable excitation frequencies, $\nu_{exc} = k_{exc}n_{Ar}$, at 200 Torr for varying Ar-He mixtures, as calculated by BOLSIG+.
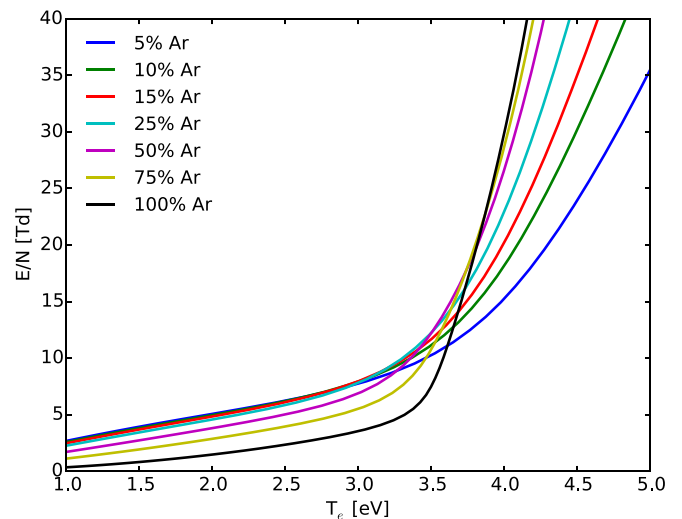
the RF discharge as an effective DC discharge, the driving frequency should be much larger than the electron energy loss frequency. This requirement is violated at the near-atmospheric pressures used in our simulations. As a result, the zero-dimensional model is benchmarked by the one-dimensional fluid model over a range of Ar-He mixtures and total pressures as outlined in Sec. IV.

In the zero-dimensional model, the electron impact rate coefficients and transport parameters are dependent on E/N, which is calculated at each time step to provide an input to BOLSIG+.[25] Reduced electric fields are calculated from the bulk plasma voltage by

$$\frac{E}{N} = \frac{V_b}{N d_e}, \tag{3}$$

where d_e is the effective distance between electrodes, and V_b is the voltage across the bulk plasma. The effective distance between electrodes accounts for the electric field increase due to the dielectric barrier

$$d_e = d - 2\delta\left(1 - \frac{\epsilon_0}{\epsilon_d}\right), \tag{4}$$

where d is the actual distance between the electrodes, and δ is the thickness of the dielectric. Bulk plasma voltages are then given by

$$V_b^2 = V_{app}^2 - (V_s + V_d)^2, \tag{5}$$

where V_{app} is the applied voltage, V_s is the potential drop in the sheaths, and V_d is the voltage drop due to charge collection at the dielectrics.[7] The voltage drop due to charge collection on the dielectric surface is as follows:

$$V_d = \frac{2\delta j}{\epsilon_d \omega}, \tag{6}$$

where j is the current density.[7] In an α-mode, the sheath voltage is as follows:

$$V_s = \frac{d_\alpha j}{\epsilon_0 \omega}, \tag{7}$$

where d_α is the sheath thickness.[7]

The sheath thickness can be estimated from the amplitude of sheath oscillation, A, by numerically solving

$$A^2\left[\left(\omega^2 - \omega_p^2 2A/d_e\right)^2 + \omega^2\nu_m^2\right] = \left(\frac{q_e V_{app}}{m_e d_e}\right)^2, \tag{8}$$

for A where ω is the driving angular frequency, ω_p is the plasma frequency, ν_m is the electron collision frequency, m_e is the electron mass, and q_e is the electron charge.[7] While the sheath thickness varies over time with the applied voltage, the peak thickness can be estimated as $d_\alpha = 2A$ (Ref. 7). At each time step, the amplitude of sheath oscillations, A, is calculated using the Newton-Raphson method. The electron collision frequency is calculated by BOLSIG+, and the plasma frequency is calculated from the electron density of the previous time-step.

The applicability of using an effective DC discharge to model the RF system is determined by first considering the RF driving angular frequency ω. If ω is much greater than the energy loss frequency for electrons, $(2m_e/M)\nu_m$, where M is the mass of the neutral atoms, then the ionization frequency, ν_i, in an RF electric field can be approximated by the ionization of a DC electric field with the magnitude reduced by a factor of $\sqrt{2}$,

$$\nu_{i,RF}(E_p) \approx \nu_{i,DC}\left(\frac{E_p}{\sqrt{2}}\right) \quad \text{for} \quad \nu_m \gg \omega \gg \left(\frac{2m_e}{M}\right)\nu_m, \tag{9}$$

where E_p is the peak applied electric field for the RF discharge.[7] For pure Ar at 200 Torr, $\omega \approx 8.5 \times 10^7$ Hz and a collision frequency of $\nu_m \approx 4.6 \times 10^{11}$ Hz calculated by BOLSIG+ for $E/N = 5$ Td provides $(2m_e/M_{Ar})\nu_m \approx 1.3 \times 10^7$ Hz, which borders the requirement for treating the RF field as a DC field with the reduced RMS magnitude. For a 1% Ar in He mixture, a collision frequency of $\nu_m \approx 2.8 \times 10^{11}$ Hz produces an electron energy loss frequency of $(2m_e/M_{He})\nu_m \approx 7.7 \times 10^7$ Hz, which does not satisfy the $\omega \gg (2m_e/M)\nu_m$ inequality. As a result, the extension of the zero-dimensional approach into a parameter space where the $\omega \gg (2m_e/M)\nu_m$ inequality is not satisfied requires a comparison to simulations from the one-dimensional fluid model to validate the zero-dimensional approach as outlined in Sec. IV. We note that while the $\omega \gg (2m_e/M)\nu_m$ inequality is not satisfied for He rich mixtures in the pressure range of 200–500 Torr, the $\nu_m \gg \omega$ inequality holds over all pressures and mixtures analyzed. We also note that this zero-dimensional approach requires minutes per simulation on an HP ENVY 750-197c Desktop, which is significantly less than the tens of hours required per simulation using the one-dimensional fluid model. The reduced computation time enables a more complete exploration of the parameter space.

IV. SIMULATIONS

Simulations are performed for the discharge chamber displayed in Fig. 3 at a pressure of 300 Torr and a peak applied voltage of 500 V with a driving angular frequency of $2\pi \times 13.56$ MHz ($V_{app} = 500\sin[\omega t]$ V). A parallel plate geometry is used in the simulations as an approximation to the centerline of the experiment geometry (Fig. 2). The Ar-He mixture is varied between 1% and 100% to analyze the effect of Ar-fraction on the metastable density. A comparison between the zero and one-dimensional models is performed in the bulk plasma at a point midway between the plates in the steady-state limit. The one-dimensional model requires roughly 2500 cycles to reach a steady-state defined by the convergence criterion outlined in Ref. 18. Zero-dimensional simulations are performed through 0.3 ms, allowing ample time for all densities and discharge parameters to reach a steady-state. A constant gas temperature of 440 K is used for all simulations, matching the experimentally measured temperatures based on observed Doppler widths.[26]

Fluorescence measurements of the discharge show the typical intensity distribution of an α-mode discharge, as displayed in Fig. 7. Simulated fluorescence is estimated by
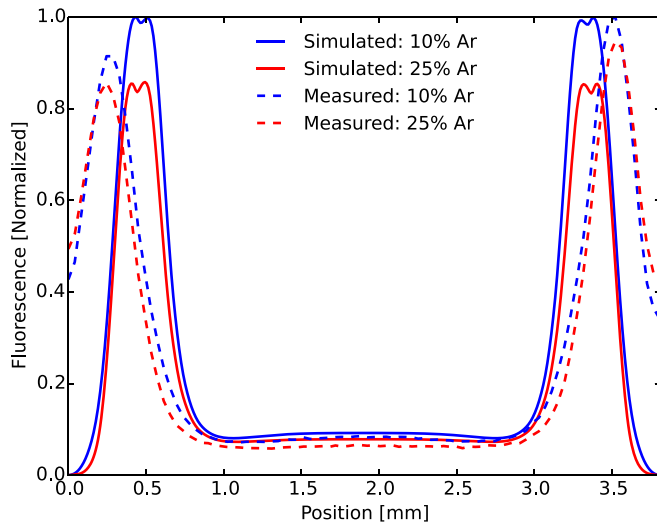
FIG. 7. Normalized fluorescence measurements and one-dimensional simulations for 10% and 25% Ar-fractions at 300 Torr. Both the measurements and simulations are indicative of an α-mode discharge.

multiplying the Ar^* densities predicted by the one-dimensional fluid model with their respective A-coefficients and averaging over one cycle. The simulated and measured fluorescence profiles are in agreement, showing an α-mode discharge with a fluorescence that varies with Ar-fraction (Fig. 7). Using the one-dimensional model, the α-mode discharge in Fig. 7 is observed to make a transition to the high current γ-mode with a peak voltage above 1400 V at 200 Torr.[27] The γ-mode is characterized by unstable behavior at high pressures[28] and is generally undesirable for use in a gas laser.[29]

A. Varying Ar-He mixture

Cycle averaged metastable density profiles from the one-dimensional simulations are displayed in Fig. 8. While the electron temperature shows a variation of approximately 0.5–1 eV during an RF cycle, the $Ar(1s_5)$ density is effectively constant throughout the cycle. Peak metastable densities on the order of 10^{12} cm^{-3} are predicted near the sheaths, with
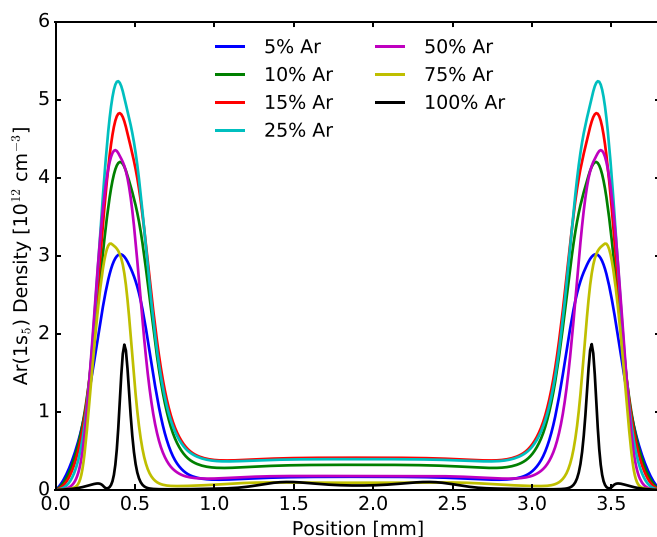
the bulk plasma densities an order of magnitude lower. As shown in Fig. 8, the 25% Ar in He mixture produces the largest metastable densities in the sheaths, with a peak of approximately 5×10^{12} cm^{-3}. In the bulk plasma, the 15% Ar-fraction produces the largest metastable densities, with magnitudes near 4×10^{11} cm^{-3}, which is on the correct order of magnitude for measured metastable densities of an Ar-He mixture in a high pressure RF-DBD.[26] While the cross-sectional area of the sheaths (bright inner region of Fig. 2) is much smaller than the area of the bulk plasma (dark inner region of Fig. 2), the $Ar(1s_5)$ densities are an order of magnitude larger. These elevated metastable densities may potentially be exploited to improve the performance of optically pumped rare gas lasers.

Electron densities are observed to increase with increasing Ar-fraction. Additionally, the peak to bulk plasma ratio increases with Ar-fraction. Electron temperatures in the bulk plasma also display an increase with increasing Ar-fraction, but an opposite trend is observed in the sheaths. Peak sheath voltages, V_s, are observed in the range of 240–250 V, providing peak sheath E/N magnitudes in the range of 125–155 Td. The elevated E/N in the sheaths is responsible for the order of magnitude increase in metastable densities relative to the bulk plasma.

A comparison of the bulk plasma electron densities simulated by the zero and one-dimensional models is displayed in Fig. 9. Both models predict similar densities and trends, increasing as the partial-pressure of Ar increases for Ar-fractions above ∼15%. The increase in electron density (and current density) with increasing Ar-fraction corresponds to a decrease in steady-state E/N for the bulk plasma due to an increase in dielectric charging and sheath voltage (Fig. 10). As the Ar-fraction increases so does the Ar_2^* density, and the dominant ionization mechanism shifts from $e^- + Ar \rightarrow 2e^- + Ar^+$ to $e^- + Ar_2^* \rightarrow 2e^- + Ar_2^+$.

The electron energy required to ionize Ar_2^* is approximately 3.4 eV, compared to the 15.8 eV required to ionize ground state Ar. However, Ar_2^* formation via $Ar(1s_5) + Ar + M \rightarrow Ar_2^* + M$ is dependent on the metastable density,

FIG. 8. One-dimensional $Ar(1s_5)$ density simulations for varying Ar-He mixtures at 300 Torr.
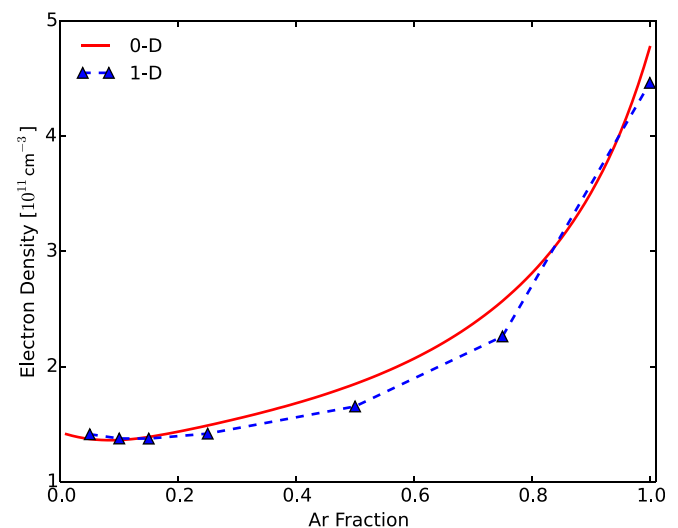

FIG. 9. Bulk plasma electron densities for varying Ar-He mixtures at 300 Torr using both the zero and one-dimensional models.
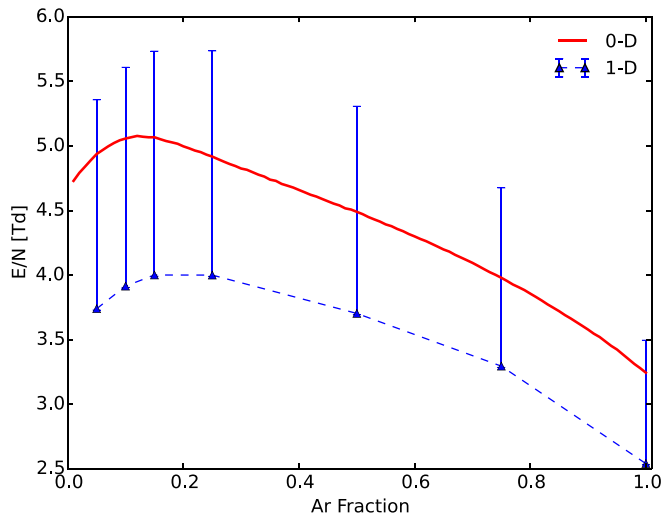
FIG. 10. Bulk plasma E/N magnitudes for varying Ar-He mixtures at 300 Torr using both the zero and one-dimensional models. The triangles represent the RMS E/N, and the bars extend to the maximum E/N attained over a cycle.
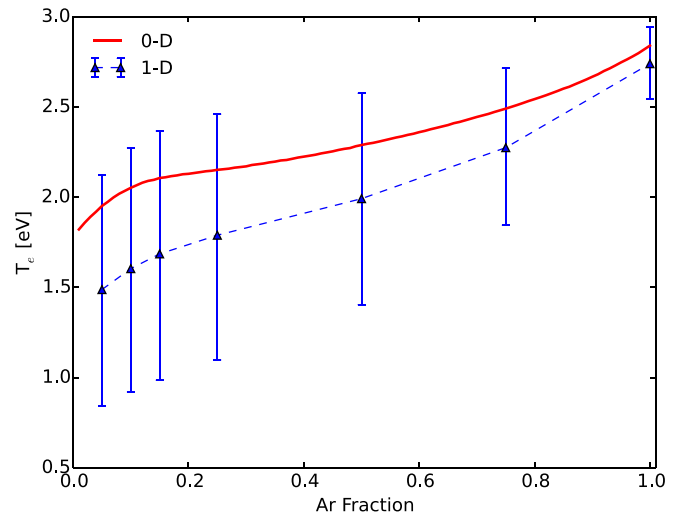

FIG. 11. Bulk plasma electron temperatures for varying Ar-He mixtures at 300 Torr using both the zero and one-dimensional models. The triangles represent the cycle-averaged T_e, and the bars correspond to the range of values obtained over a cycle.

which requires electron energies of 11.6 eV for production through $e^- + Ar \rightarrow e^- + Ar(1s_5)$. Therefore, a better comparison of the energies required for the two different ionization mechanisms is between the energy required for $Ar(1s_5)$ excitation, 11.6 eV, and the energy required for ionization of ground state Ar, 15.8 eV, resulting in a difference of 4.2 eV. The reduction in energy required for ionization via $e^- + Ar_2^* \rightarrow 2e^- + Ar_2^+$ allows for a lower steady-state E/N at larger Ar-fractions (Fig. 10), which in turn requires a larger electron density (current density) to reach the steady-state (Fig. 9).

While stepwise ionization via $e^- + Ar(1s_5) \rightarrow 2e^- + Ar^+$ has been shown to be the dominant ionization mechanism at low pressures ($\sim$1 Torr),[30] dimer ionization through $e^- + Rg_2^* \rightarrow 2e^- + Rg_2^+$ has been shown to dominate ionization for both $Rg = Ar$ and $Rg = He$ at atmospheric pressures.[31,32] For $T_e \approx 2$ eV, predicted for the 50% Ar-fraction at 300 Torr, the ionization rate coefficient for $e^- + Ar(1s_5) \rightarrow 2e^- + Ar^+$, calculated by BOLSIG+ using the cross section from Ref. [33], is approximately 7×10^{-10} cm^3/s. The rate coefficient for ionization via $e^- + Ar_2^* \rightarrow 2e^- + Ar_2^+$, calculated by BOLSIG+ using the cross section from Ref. [34], is approximately two orders of magnitude larger: 4×10^{-8} cm^3/s. This difference in rate coefficients indicates that dimer ionization will be larger than stepwise ionization of $Ar(1s_5)$ if the Ar_2^* density is within an order of magnitude of the $Ar(1s_5)$ density, which occurs for most of the mixtures and pressures in this analysis.

The bulk plasma electron temperature increases with increasing Ar-fraction (Fig. 11), in contrast to the E/N. This increase in T_e with a reduction of E/N can be described by Fig. 6, where the mapping of E/N to T_e is shown to be mixture dependent. For E/N magnitudes below 6 Td, T_e increases as the Ar-fraction increases. The electron temperature (or E/N) predicted using the zero-dimensional DC approach is larger than the average (RMS) values of the one-dimensional RF model but less than the peaks. While the time-varying electric field in the one-dimensional model allows the electron temperature (E/N) to vary over a cycle, the DC approach maintains a constant electron temperature (E/N) at steady-state.

In the one-dimensional RF model, ionization rates vary over the RF cycle following the change in electron temperature (or E/N). The zero-dimensional effective DC approach maintains a constant ionization rate due to a constant electron temperature (E/N) at steady-state. Ionization rates for the two approaches are displayed in Fig. 12, which shows an increase in ionization rates as the Ar-fraction is increased, matching the trend in electron density. While the ionization rates for the one-dimensional RF model vary over the cycle, the cycle averaged values are close in magnitude to the constant ionization rates from the zero-dimensional effective DC model. Differences in the ionizations rates correspond to differences in electron loss rates, which are functions of T_e and the electron/ion densities.

In the steady-state, electron loss rates as a function of Ar-fraction are equal to the electron production rates displayed in
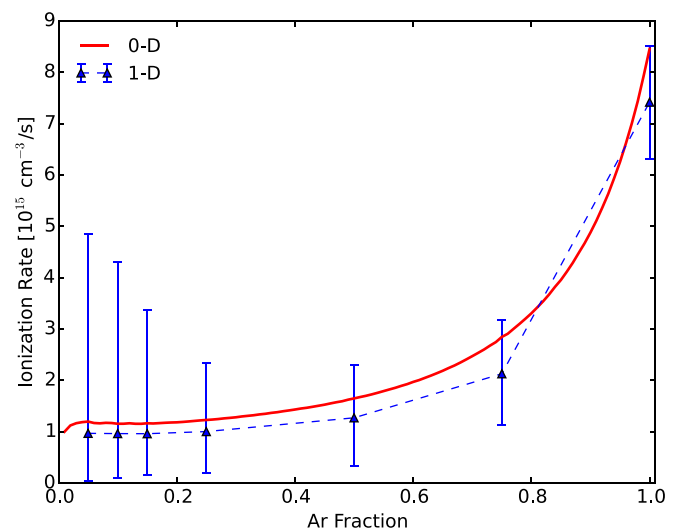

FIG. 12. Bulk plasma ionization rates for varying Ar-He mixtures at 300 Torr using both the zero and one-dimensional models. The triangles represent the cycle-averaged ionization rates, and the bars correspond to the range of values obtained over a cycle.

Fig. 12. For the discharge conditions and cavity geometry of the RF-DBD at 300 Torr, the electron loss rates are dominated by dissociative recombination of Ar_2^+ via $Ar_2^+ + e^- \to Ar(h.l.) + Ar$. The Ar_2^+ density is predicted to increase with increasing Ar-fraction, which causes an increase in the electron loss rates. This increase in electron loss rates with increasing Ar-fraction corresponds to an increase in T_e (Fig. 11), which is opposite to the trend predicted for a microwave resonator-driven microplasma at near atmospheric pressures.[9] The difference in trends is due to disparate discharge conditions and geometry, where the microwave resonator-driven microplasma is produced in a $\sim100\ \mu m$ discharge gap by a GHz driving frequency, as opposed to the 3.8 mm discharge gap and 13.56 MHz driving frequency for the RF-DBD. A reduced cavity size for the microplasma enhances ambipolar diffusion loss rates, which decrease with increasing Ar-fraction as a result of a reduced ion mobility in a background gas of Ar compared to He.[17,35] For discharges where ambipolar diffusion is the primary loss mechanism, the electron loss frequencies will decrease as the Ar-fraction increases.

The zero and one-dimensional models predict a similar trend in metastable density, with peaks near 15% Ar in He followed by a reduction in density as Ar-fraction is increased (Fig. 13). Metastable density trends follow the trends in E/N, which also show peaks near the 15% Ar-fraction. Excitation rate coefficients for metastable production via $e^- + Ar \to e^- + Ar(1s_5)$ are highly dependent on E/N, which explains the similarity of the E/N and $Ar(1s_5)$ density trends over Ar-fraction. The trend of $Ar(1s_5)$ density with Ar-fraction at 300 Torr matches the general trend measured for a microwave resonator-driven microplasma.[9] However, the metastable density magnitudes for the RF-DBD are approximately two orders of magnitude lower, and the peak $Ar(1s_5)$ density occurs at a larger Ar-fraction for the RF-DBD.

B. Varying pressure

To analyze the effect of pressure on the metastable density, an Ar-fraction of 15% is simulated for pressures in the range of 200–500 Torr. As pressure is increased, the
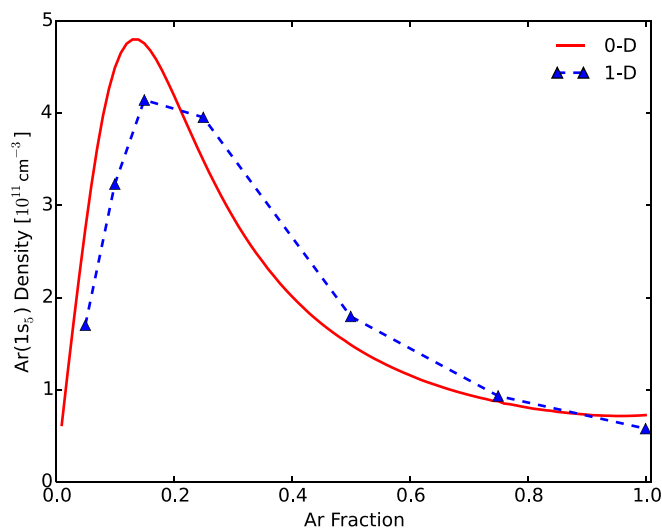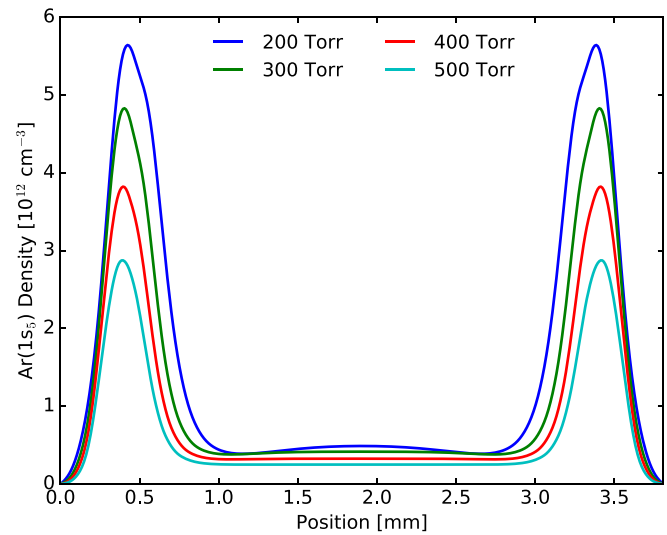

FIG. 14. One-dimensional $Ar(1s_5)$ density simulations for varying pressures in a 15% Ar in He mixture.

electron loss rate due to ambipolar diffusion decreases. Additionally, the role of ionization through $e^- + Ar_2^* \to 2e^- + Ar_2^+$ increases with pressure, accounting for an overall decrease in steady-state T_e and E/N. The electron/current density required to reduce the initial E/N to the steady-state E/N decreases with pressure due to an increased gas density that reduces the initial E/N magnitude. The decrease in electron density and electron temperature combined with an increase in the metastable loss rates, primarily through excimer formation via $Ar(1s_5) + Ar + M \to Ar_2^* + M$, causes an overall decrease in metastable density with increasing pressure, as displayed in Fig. 14. The quadratic dependence of the metastable loss rates on the pressure is larger than the linear increase in Ar density assisting with metastable production rates through $e^- + Ar \to e^- + Ar(1s_5)$, which would decrease the steady-state metastable density even if the electron density and temperature were to remain constant.

Bulk plasma electron densities for the zero-dimensional DC model are displayed with the one-dimensional results in Fig. 15. Both models predict a nearly constant electron density

FIG. 13. Bulk plasma $Ar(1s_5)$ densities for varying Ar-He mixtures at 300 Torr using both the zero and one-dimensional models.
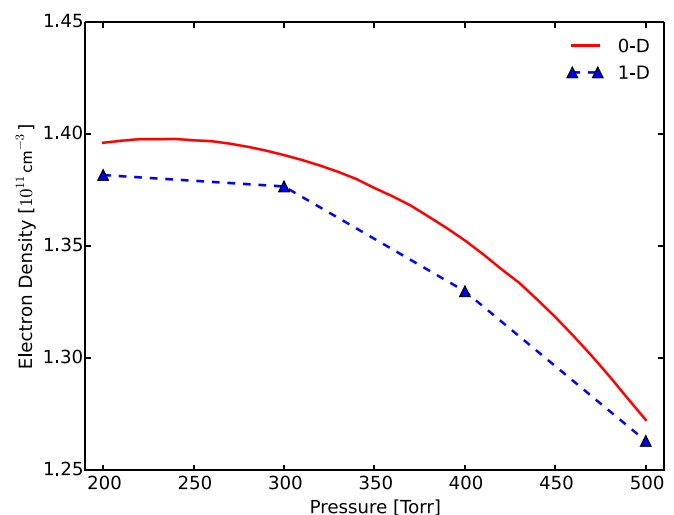

FIG. 15. Bulk plasma electron densities for varying pressures in a 15% Ar in He mixture using both the zero and one-dimensional models.
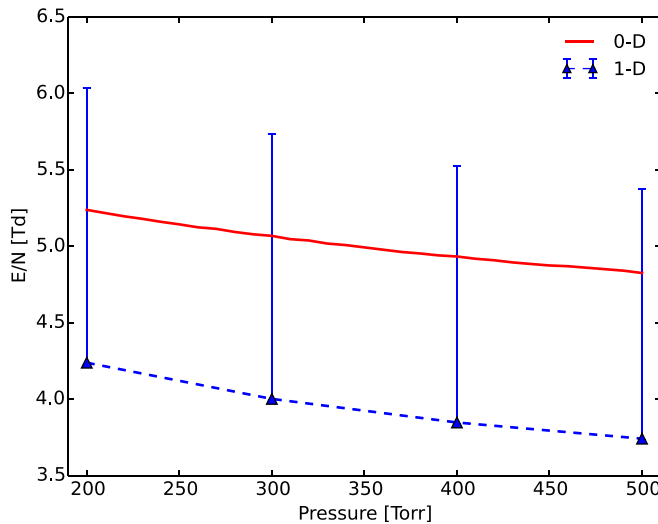
FIG. 16. Bulk plasma E/N magnitudes for varying pressures in a 15% Ar in He mixture using both the zero and one-dimensional models. The triangles represent the RMS E/N and the bars extend to the maximum E/N attained over a cycle.

from 200 to 300 Torr followed by a decrease from 300 to 500 Torr. The electron density is slightly overestimated by the zero-dimensional model at all pressures. A small decrease in E/N and T_e is observed as pressure is increased, with both models in agreement (Figs. 16 and 17). The T_e (or E/N) magnitude for the zero-dimensional DC approach is between the average (RMS) and maximum of the time-varying one-dimensional approach. A decreasing T_e with increasing pressure matches the trends calculated from measurements of a bare electrode RF discharge at a constant current density.[36] At a constant current density, Ref. 36 shows an increase in electron density with increasing pressure, which is opposite to our predicted trend for an RF-DBD at a constant applied voltage. This difference results from a constant current density as opposed to a constant applied voltage, which requires different electron densities to reach steady-state as the pressure is varied.
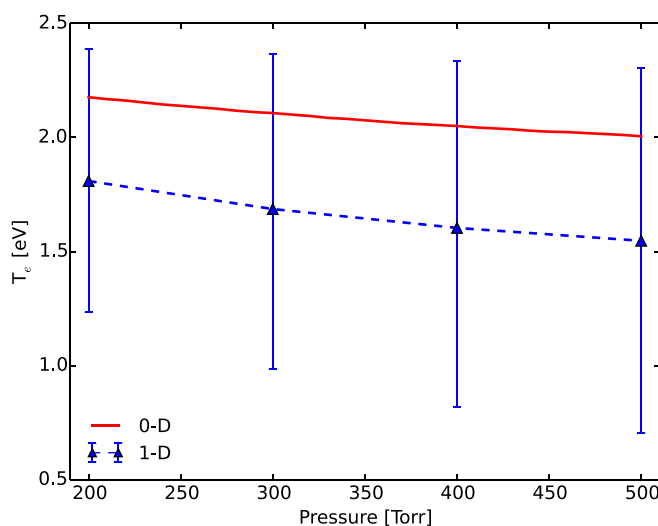

FIG. 17. Bulk plasma electron temperatures for varying pressures in a 15% Ar in He mixture using both the zero and one-dimensional models. The triangles represent the cycle-averaged T_e and the bars correspond to the range of values obtained over a cycle.
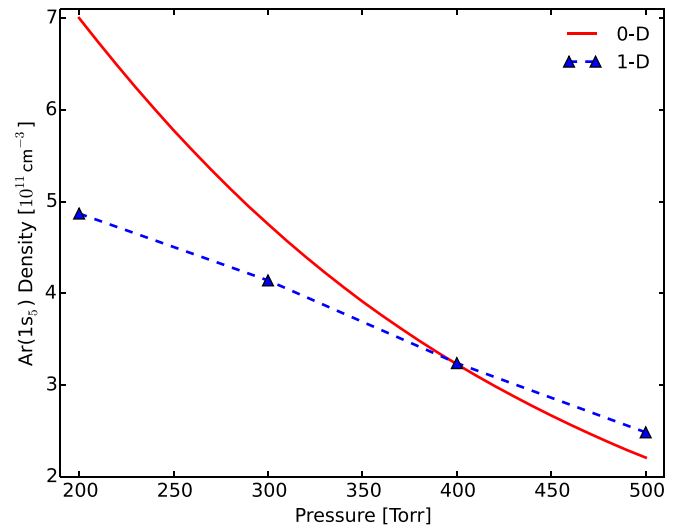

FIG. 18. Bulk plasma $Ar(1s_5)$ densities for varying pressures in a 15% Ar in He mixture using both the zero and one-dimensional models.

The $Ar(1s_5)$ density is overestimated by the zero-dimensional approach for pressures below 400 Torr (Fig. 18). While the one-dimensional model predicts a decrease from 4.9×10^{11} to 2.5×10^{11} cm^{-3} as the pressure is increased from 200 to 500 Torr, the zero-dimensional model predicts a factor of 3 decrease from 7.0×10^{11} to 2.2×10^{11} cm^{-3}. However, both models show the same trend with decreasing metastable density as the pressure is increased, which matches the measured trends for high pressure RF-DBDs and microwave resonator-driven microplasmas.[9,26]

Extending the zero-dimensional simulations to the entire range of Ar-He mixtures and pressures provides the bulk plasma metastable density profile displayed in Fig. 19. The trend of $Ar(1s_5)$ as a function of Ar-fraction displayed in Fig. 13 can be seen for pressures near 300 Torr in Fig. 19. As pressure is increased, three-body collisions via $Ar(1s_5) + Ar + Ar \rightarrow Ar_2^* + Ar$, which is estimated to have twice the rate constant of the $Ar(1s_5) + Ar + He \rightarrow Ar_2^* + He$ analog,[3] cause a drastic decrease in metastable densities for Ar rich
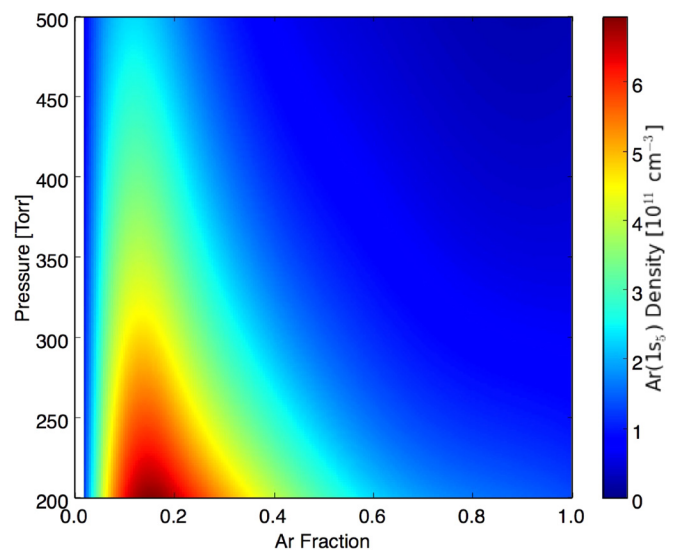

FIG. 19. Bulk plasma $Ar(1s_5)$ densities for varying pressures and Ar-He mixtures using the zero-dimensional effective DC model.

mixtures. Increased Ar_2^* production at elevated pressures causes the peak E/N to occur at lower Ar-fractions due to ionization contributions from $e^- + Ar_2^* \rightarrow 2e^- + Ar_2^+$. This shift in E/N corresponds to a shift in metastable production, causing the peak metastable density to occur at lower Ar-fractions as the pressure is increased. At 200 Torr, the peak metastable density occurs near a 15% Ar-fraction, while the peak is shifted to approximately 10% at 500 Torr.

V. CONCLUSIONS

Simulations of an α-mode radio frequency dielectric barrier discharge are performed for a variety of Ar-He mixtures and gas pressures. The results from a one-dimensional fluid model are compared to a zero-dimensional effective DC model in the bulk plasma, showing general agreement over Ar-fractions ranging from 5% to 100% and pressures between 200 and 500 Torr. The agreement between the two models indicates that the zero-dimensional effective DC model provides a valid approach to modeling the bulk plasma of a high pressure RF-DBD.

Peak metastable densities at 300 Torr are observed near a 15% Ar in He mixture for the geometry of the discharge chamber used in the simulations, corresponding to the peak E/N for the varying mixtures. Electron temperature and electron density are observed to increase with increasing Ar-fraction. Metastable densities are shown to decrease with increasing pressure due to a reduction in E/N and a quadratic increase in metastable loss rates through excimer formation: $Ar(1s_5) + Ar + M \rightarrow Ar_2^* + M$. The decrease in bulk plasma E/N is primarily caused by an increase in ionization through $e^- + Ar_2^* \rightarrow 2e^- + Ar_2^+$, which requires significantly less energy than ionization through $e^- + Ar \rightarrow 2e^- + Ar^+$.

Additionally, the peak $Ar(1s_5)$ density shifts from an Ar-fraction of approximately 15% at 200 Torr to 10% at 500 Torr. The increased excimer formation rate at elevated pressures raises Ar_2^* densities for He rich mixtures, causing the peak E/N to occur at lower Ar-fractions as the pressure is increased. This shift in E/N corresponds to a shift in metastable production and peak density.

In the pressure range of 200–500 Torr, the metastable density for an α-mode radio frequency dielectric barrier discharge using an Ar-He mixture peaks at 200 Torr with 15% Ar in He. While the metastable density decreases with increasing pressure, the gas pressure must also be taken into account when mapping to output intensities for an optically pumped rare gas laser. Both the diode pump absorption linewidth and spin orbit mixing rate via $Ar(2p_9) + M \rightarrow Ar(2p_{10}) + M$ increase with increasing pressure, requiring further calculations to maximize the laser performance for this discharge scenario.

ACKNOWLEDGMENTS

[1]J. Han, M. C. Heaven, G. D. Hager, G. B. Venus, and L. B. Glebov, in *SPIE LASE* (International Society for Optics and Photonics, 2014), p. 896202.
[2]W. Rawlins, K. Galbally-Kinney, S. Davis, A. Hoskinson, J. Hopwood, and M. Heaven, Opt. Express **23**, 4804 (2015).
[3]A. Demyanov, I. Kochetov, and P. Mikheyev, J. Phys. D: Appl. Phys. **46**, 375202 (2013).
[4]R. A. Haas, Phys. Rev. A **8**, 1017 (1973).
[5]A. Napartovich, Plasmas Polym. **6**, 1 (2001).
[6]A. Fridman, A. Chirokov, and A. Gutsol, J. Phys. D: Appl. Phys. **38**, R1 (2005).
[7]Y. P. Raizer, M. N. Shneider, and N. A. Yatsenko, *Radio-Frequency Capacitive Discharges* (CRC Press, 1995).
[8]Z. Yang, G. Yu, H. Wang, Q. Lu, and X. Xu, Opt. Express **23**, 13823 (2015).
[9]A. R. Hoskinson, J. Gregório, J. Hopwood, K. Galbally-Kinney, S. J. Davis, and W. T. Rawlins, J. Appl. Phys. **119**, 233301 (2016).
[10]D. Emmons and D. Weeks, J. Appl. Phys. **121**, 203301 (2017).
[11]T. Holstein, Phys. Rev. **83**, 1159 (1951).
[12]T. Holstein, Phys. Rev. **72**, 1212 (1947).
[13]G. Hagelaar and L. Pitchford, Plasma Sources Sci. Technol. **14**, 722 (2005).
[14]A. Ward, J. Appl. Phys. **33**, 2789 (1962).
[15]A. Blanc, J. Phys. Theor. Appl. **7**, 825 (1908).
[16]M. A. Biondi and L. M. Chanin, Phys. Rev. **122**, 843 (1961).
[17]W. Lindinger and D. Albritton, J. Chem. Phys. **62**, 3517 (1975).
[18]D. P. Lymberopoulos and D. J. Economou, J. Appl. Phys. **73**, 3668 (1993).
[19]J. Boeuf and L. Pitchford, Phys. Rev. E **51**, 1376 (1995).
[20]T. Farouk, B. Farouk, D. Staack, A. Gutsol, and A. Fridman, Plasma Sources Sci. Technol. **15**, 676 (2006).
[21]E. Gogolides and H. H. Sawin, J. Appl. Phys. **72**, 3971 (1992).
[22]Plasma Module User's Guide, COMSOL Multiphysics™ v. 5.2a, Stockholm, Sweden (2016).
[23]D. L. Scharfetter and H. K. Gummel, IEEE Trans. Electron Devices **16**, 64 (1969).
[24]S. Pancheshnyi, B. Eismann, G. Hagelaar, and L. Pitchford, see http://www.zdplaskin.laplace.univ-tlse.fr for Computer code ZDPlasKin, University of Toulouse, LAPLACE, CNRS–UPS–INP, Toulouse, France (2008).
[25]B. Eismann, "Etude numérique et théorique des phénomènes liés aux hautes pressions dans les microdécharges," Ph.D. thesis (Université de Toulouse, Université Toulouse III-Paul Sabatier, 2011).
[26]B. Eshel, C. A. Rice, and G. P. Perram, J. Quant. Spectrosc. Radiat. Transfer **179**, 40 (2016).
[27]D. J. Emmons, "Analysis of Ar(1s5) metastable populations in high pressure argon-helium gas discharges," Ph.D. thesis (Air Force Institute of Technology, 2017).
[28]N. Balcon, G. Hagelaar, and J. Boeuf, IEEE Trans. Plasma Sci. **36**, 2782 (2008).
[29]A. Garscadden, M. J. Kushner, and J. G. Eden, IEEE Trans. Plasma Sci. **19**, 1013 (1991).
[30]C. Ferreira, J. Loureiro, and A. Ricard, J. Appl. Phys. **57**, 82 (1985).
[31]W. Van Gaens and A. Bogaerts, J. Phys. D: Appl. Phys. **46**, 275201 (2013).
[32]X. Yuan and L. L. Raja, IEEE Trans. Plasma Sci. **31**, 495 (2003).
[33]A. V. Phelps, Phelps database, 2008.
[34]K. McCann, M. Flannery, and A. Hazi, Appl. Phys. Lett. **34**, 543 (1979).
[35]J. Madson and H. Oskam, Phys. Lett. A **25**, 407 (1967).
[36]M. Moravej, X. Yang, G. Nowling, J. Chang, R. Hicks, and S. Babayan, J. Appl. Phys. **96**, 7011 (2004).